

Missing or Underrated Super-emitters of Nitrogen Oxides in China Exposed from Space

Pengfei Li (✉ lpf_zju@163.com)

Hebei Agricultural University

Yuqing Pan

Hebei Agricultural University

Lei Duan

Hebei Agricultural University

Mingqi Li

Hebei Agricultural University

Pinqing Song

Hebei Agricultural University

Nan Xv

Hebei Agricultural University

Jing Liu

Hebei Agricultural University

Shaozhuo Li

Hebei Agricultural University

Yifei Le

Zhejiang Chinese Medical University

Cui Wang

Zhejiang Chinese Medical University

Jingjun Ma

Hebei Agricultural University

Xin Zhou

Hebei Agricultural University

Wei Wang

Hebei Agricultural University

Yali Shi

Hebei Agricultural University

Wei Su

Hebei Agricultural University

Gang Wang

Hebei Agricultural University

Liqiang Wang

Zhejiang University

Xue Chen

Zhejiang University

Yan Xia

Zhejiang University

Linhui Jiang

Zhejiang University

Yibo Zhang

Zhejiang University

Mengying Li

Zhejiang University

Zhen Li

Zhejiang University

Weiping Liu

Zhejiang University

Shaocai Yu

Zhejiang University

Daniel Rosenfeld

The Hebrew University of Jerusalem

John H. Seinfeld

Departments of Environmental Science and Engineering & Chemical Engineering

<https://orcid.org/0000-0003-1344-4068>

Article

Keywords: nitrogen oxides, air pollution

Posted Date: April 20th, 2021

DOI: <https://doi.org/10.21203/rs.3.rs-417977/v1>

License:   This work is licensed under a Creative Commons Attribution 4.0 International License.

[Read Full License](#)

1 **Missing or Underrated Super-emitters of Nitrogen Oxides in China**
2 **Exposed from Space**

3 Yuqing Pan¹, Lei Duan¹, Mingqi Li¹, Pinqing Song¹, Nan Xv¹, Jing Liu¹, Shaozhuo Li¹, Yifei Le², Cui
4 Wang^{2*}, Jingjun Ma¹, Xin Zhou¹, Wei Wang¹, Yali Shi¹, Wei Su¹, Gang Wang¹, Liqiang Wang³, Xue
5 Chen³, Yan Xia³, Linhui Jiang³, Yibo Zhang³, Mengying Li³, Zhen Li³, Weiping Liu³, Shaocai Yu^{3,5*},
6 Daniel Rosenfeld⁴, John H. Seinfeld⁵, Pengfei Li^{1*}

7 ¹College of Science and Technology, Hebei Agricultural University, Baoding, Hebei 071000, P.R. China

8 ²College of Life Science, Zhejiang Chinese Medical University, Hangzhou 310053, Zhejiang, P.R. China

9 ³Research Center for Air Pollution and Health; Key Laboratory of Environmental Remediation and Ecological Health,
10 Ministry of Education, College of Environment and Resource Sciences, Zhejiang University, Hangzhou, Zhejiang 310058,
11 P.R. China

12 ⁴Institute of Earth Science, The Hebrew University of Jerusalem, Jerusalem, Israel

13 ⁵Division of Chemistry and Chemical Engineering, California Institute of Technology, Pasadena, CA 91125, USA

14

15

16 *Correspondence to: Pengfei Li (lpf_zju@163.com);

17 Cui Wang (wangcui198506@163.com);

18 Shaocai Yu (shaocaiyu@zju.edu.cn).

19

20

21

22

23

24

25

26

27

28

29

To be submitted to
Nature Communication

30 **Abstract**

31 Nitrogen oxides ($\text{NO}_x \equiv \text{NO} + \text{NO}_2$) play a central role in air pollution. Super-emitters present unique opportunities for
32 emission mitigation in China and beyond. They comprise intensive industrial facilities (e.g., power or chemical plants), less
33 than $1 \times 1 \text{ km}^2$ with high NO_x plumes, dominating localized concentrations within a limited geographical scope. However,
34 identification of super-emitters typically challenges emission mitigation due to insufficient spatiotemporal resolution. Here
35 we map NO_x emissions using an efficient, super-resolution ($1 \times 1 \text{ km}^2$) inverse model based on whole-year TROPOMI
36 satellite observations. Our map offers unique insights on nationwide NO_x super-emitters. We resolve 1625 super-emitters in
37 virtually every corner in China, even in remote and mountainous zones, which we trace back to either an industrial hotspot or
38 a cluster (i.e., an industrial park). A state-of-the-art bottom-up emission inventory MEICv1.3 largely (67%) agrees with our
39 results within a factor of two for cities. However, that inventory does not identify these super-emitters, particularly
40 underestimating one-third of the emissions by at least an order of magnitude. Even, nearly up to three-quarter super-emitters
41 are found to be displaced or missing. Moreover, traditional top-down inverse methods do not effectively detect such super-
42 emitters. Here we show it is necessary to address the NO_x budget by revisiting super-emitters on a large scale. Integrating the
43 results we obtain here with a multi-tiered observation system can lead to identification and mitigation of anomalous NO_x
44 emissions.

45 **Introduction**

46 Nitrogen oxides ($\text{NO}_x \equiv \text{NO} + \text{NO}_2$) play a central role in the formation of fine particular matter and ozone and have
47 implications for climate change, human health, and life expectancy¹⁻⁴. They are typically emitted by all combustion
48 processes, particularly industrial activities (e.g., power or chemical plants)⁵⁻⁸. China is a case in point. There is a heavy-tail
49 distribution of NO_x emission sources in a number of localized regions^{9,10}, where a few sources (so-called super-emitters)
50 generally emit highly concentrated NO_x plumes and might even dominate localized emissions with limited geographical
51 extent (i.e., $\sim 1 \times 1 \text{ km}^2$). Hence, unique opportunities for mitigation are presented by super-emitters, particularly by those
52 due to leaks and abnormal operating conditions^{11,12}.

53 However, efforts to guide super-emitter mitigation are complicated by large inconsistencies between emission estimates¹³⁻¹⁶.
54 This is primarily because these inventories are generally designed at the regional scale rather than localized super-emitters.
55 For instance, the foundations of bottom-up inventories, such as activity data and emission factors, are often outdated, sparse,
56 and unrepresentative for super-emitters^{5,7,17,18}. By comparison, top-down attempts relying on relatively accurate and up-to-
57 date measurements present a more promising future⁶. Nevertheless, there is a dearth of available regular measurements for
58 the super-emitters¹⁹. Field campaigns are also spatially sparse and temporally infrequent, thus inapplicable for the super-
59 emitters distributed over a large scale.

60 For decades, satellite measurements have provided spatial patterns and magnitude of tropospheric NO₂ vertical column
61 densities (VCDs) on a global scale, central to improving our knowledge of the NO_x emission budget^{1,6,20}. However, the
62 ability to detect super-emitters has been limited by pixels far larger than $1 \times 1 \text{ km}^2$ ²¹. Finally, the emissions attributed to the
63 NO_x super-emitters have not been well isolated and evaluated nationwide.

64 The TROPospheric Monitoring Instrument (TROPOMI) on the Sentinel-5 Precursor has an unprecedented spatial resolution
65 of up to $3.5 \times 7 \text{ km}^2$ ($3.5 \times 5.5 \text{ km}^2$ from August 2019 onward) and a high signal-to-noise ratio^{7,13}. A representative top-
66 down method using a CTM and a Kalman Filter has tested the TROPOMI measurements at a sacrifice of spatial resolution
67 (i.e., $\sim 0.25^\circ \times 0.25^\circ$)²², consequently focusing only on regional issues. A recent study preserved the benefit of its high
68 spatial resolution and experimentally exposed a few large emission sources on a national scale⁷. However, the original
69 TROPOMI's resolution ($3.5 \times 5.5 \text{ km}^2$) still has a crucial gap in the scale of the localized super-emitters ($\sim 1 \times 1 \text{ km}^2$).

70 Here we develop an efficient, super-resolution (i.e., from $3.5 \times 5.5 \text{ km}^2$ to $1 \times 1 \text{ km}^2$) inverse model by capitalizing on a
71 whole year of daily TROPOMI measurements (Methods). The retrievals of the NO_x VCDs are supported by a state-of-the-art
72 CTM (i.e., the WRF-CMAQ model). To prevent the super-emitters from being omitted, a key advance of this model is to
73 take into account the nonlinear NO_x VCD-Transport-Lifetime-Emission relationships and to integrate an oversampling
74 method^{7,14}. The objective is to provide the first systematic survey of the NO_x emission distributions at the super-resolution,
75 with a focus on geo-locating and quantifying the super-emitters nationwide, down to the industrial hotspots or parks. Our
76 survey is used to benchmark a state-of-the-art emission inventory MEICv1.3 (the Multi-resolution Emission Inventory for
77 China) and also a state-of-the-art top-down product. This will help fill an important gap in scale and re-evaluate the NO_x
78 budget and hotspots in China.

79 **Identification of super-emitters**

80 An oversampling approach was applied to exploit the variable spatial coverage of the satellite pixels (Methods). As a result,
81 we achieved the super-resolution (i.e., from $3.5 \times 5.5 \text{ km}^2$ to $1 \times 1 \text{ km}^2$) tropospheric NO_x VCDs based on the TROPOMI
82 measurements in China (Fig. 1a). We also zoomed in on five sub-regions (including Northwest, Northeast, North, Southwest,
83 East, and South China) (Figs. 1b ~ 1g). On this basis, the consequent NO_x emission map was derived by an efficient,
84 compatible top-down inverse model (Fig. S1). In theory, this set of maps (Fig. 1 and Fig. S1) is distinct from previous
85 outcomes obtained from early satellite-based surveys (e.g., those based on the OMI or TROPOMI measurements)^{13,14,23}. This
86 is solely attributed to major improvements in the model developed here, which is of hyperfine resolution and takes
87 meteorological and chemical effects into account (Methods; Supplementary Information). An illustrative comparison is
88 explained in the next section. We isolated and identified 1625 hotspots (Fig. 1) that are inventoried in Supplementary Table
89 1 only if they could be resolved unambiguously on the basis of the maps alone without the need for a priori knowledge. Each
90 exhibited a prominent localized (i.e., $1 \times 1 \text{ km}^2$) NO_x enhancement regarding both VCDs and emissions.

91 Spatially, we found that these super-emitters are scattered on every corner in China, even in remote zones close to the
92 frontiers (e.g., Northwest and Southwest China) (Fig. 1). As expected, such super-emitters concentrated over North, East,
93 and South China. By combining the Landsat 8 images, the identified super-emitters can be classified into two classes:
94 industrial hotspots and industrial parks. They can be linked to the super-emitters typically containing individual point
95 sources or intensive industrial facilities. Illustrative examples are shown in Fig. 2 and Fig. S3, and detailed spatial
96 information is highlighted in Fig. S2. The 936 hotspots in the class of industrial hotspots were consistently found to be
97 associated with isolated industrial factories or power plants with one or more chimneys, as presented in the visible images.
98 For instance, a typical localized NO_x emission maximum was found in a remote desert area in Northwest China (Fig. 2a),
99 coinciding spatially with a large industrial factory (Zeketai, Northwest China), as shown in the satellite image. It was
100 adjacent to a small city (i.e., Xinyuan in Xinjiang Province) dominated by residential areas, but with much lower NO_x
101 distributions and emissions. Longzhudou (East China) (Fig. 2b) and Huaxin (Southwest China) (Fig. S3a) were similar
102 examples of industrial hotspots. They were also planted in mountainous areas but close to medium-sized cities (Ningde in
103 Fujian Province and Lhasa in Tibet). The Jincheng Steel Group, located in North China, is a key base of the iron and steel
104 industry (Fig. 2c). NO_x emissions associated with coal-fired power plants were also identified, for example, in Rundajianeng
105 (Northwest China) (Fig. 2d) and Mudanjiang (Northeast China) (Fig. S3b).

106 The second class, that of industrial parks, is linked to aggregative zones with massive industrial facilities but limited
107 geographical extent (i.e., $1 \times 1 \text{ km}^2$), for which nearly 700 parks were detected. They were mostly associated with chemistry
108 and manufacturing industries, such as oil and gas, iron and steel, and foundry production. Well-isolated examples include the
109 parks in Baitong (Northwest China) (Fig. 2e), Shizuishan (North China) (Fig. 2f) Zhongluan (North China) (Fig. S3c), and
110 Beiyong (Northeast China) (Fig. S3d). These super-emitters were clearly detected in the set of the maps, despite already large
111 background concentrations. Chemical industrial parks, due to their large production, were often found to be geographically
112 close to their distribution market. Nanbao (East China) (Fig. 2g) and Jiaochuan (East China) (Fig. S3e) are the representative
113 and bordered on the Beijing-Tianjin-Hebei region and the Yangtze River Delta region, respectively. Many industrial parks
114 were also found near raw-material-related industries (e.g., oil fields and coal mines), thus conducive to building an agile
115 supply chain. Daqing (Northeast China) (Fig. 2h) is an archetype of such a super-emitter, which is next to the famous Daqing
116 Oilfield and railway stations. Moreover, such examples are abundant. For instance, the large petrochemical industrial parks,
117 such as Longmen (Northwest China) (Fig. S3f) and Shengbang (Northwest China) (Fig. S3g), were also close to the coal
118 bases (i.e., the Hancheng Coal Mine and the Shenmu Coal Mine).

119 Commonly, rural regions were also found with enhanced NO_x VCDs and emissions. These regions correspond to, for
120 example, residential areas and small-scale manufacture clusters, such as Jiqingbao (North China) (Fig. S4a), Pangjing (East
121 China) (Fig. S4b), and Chetian (Southwest China) (Fig. S4c). The primary NO_x sources might be attributed to scattered coal
122 combustion^{24,25}. Nevertheless, it was difficult to link those sources with clear, well-isolated super-emitters. Also, NO_x
123 emissions in cities represent a substantial part of the total atmospheric NO_x budget. Megacities, such as Beijing (Fig. S4d),

124 Shanghai (Fig. S4e), Guangzhou (Fig. S4f), and Shenzhen (Fig. S4g), are the cases in point. We emphasized that, from a
125 narrower spatial perspective (i.e., $\sim 10 \times 10 \text{ km}^2$), small-medium cities, such as Lhasa (Southwest China) (Fig. S4h),
126 Shizuishan (Northwest China) (Fig. S4i), and Yongan (South China) (Fig. S4j), are no exception. The main sources can be
127 consistently related to urban transportation, which, however, are too diffuse to emerge as individual super-emitters in our
128 maps. In addition, the one-year average of satellite detections was generally difficult to capture discontinuous and
129 instantaneous biomass burning. Thus, hotspots dominated by biomass burning were excluded from this study.

130 **Assessment of super-emitters**

131 We have compared the emission fluxes from all the super-emitters and 370 cities in China in our model with those in the
132 state-of-the-art bottom-up emission inventory MEICv1.3 (Methods, Supplementary Information) (Supplementary Table 1).
133 For 67% of the cities, the emission fluxes agreed within a factor of two (85% within a factor of three) and, importantly, when
134 all large and medium-sized cities were considered, no major bias emerged. Note that, compared to our results, the inventory
135 often underestimated the NO_x emissions in remote small-sized cities significantly (by more than a factor of five)
136 (Supplementary Table 1). Therein some isolated super-emitters (i.e., industrial hotspots or parks), such as Hejing (Northwest
137 China), Geermu (Northwest China), and Luopu (Northwest China), were directly missed (Figs. S5a ~ S5c). It should be
138 emphasized that, in turn, our estimates of NO_x emissions in several megacities, such as Shanghai and Shenzhen, are less than
139 those in MEICv1.3 to some extent (i.e., $> -20\%$). This could be attributed to persistent air pollution controls in China since
140 2013²⁶. In contrast, it was immediately clear that the emission fluxes of the super-emitters were largely underestimated in
141 MEICv1.3, irrespective of their classes. Of all the identified super-emitters, only 35% agreed within a factor of three and,
142 more importantly, only 72% within one order of magnitude. Overall, they exhibit a heavy-tail distribution, indicating that 20%
143 of the identified hotspots were responsible for 40% of all the detected super emissions (Fig. 3 and Supplementary Table 1).
144 Compared to MEICv1.3, this satellite survey reveals three kinds of super-emitters. First, 460 super-emitters are identified
145 owing to a nearby localized maximum in the bottom-up inventory, despite exceptionally low emission fluxes. Representative
146 examples were presented in Fig. 3, including Maligou (Northwest China) (Fig. S5d) for an industrial hotspot and Sanbaotun
147 (Northeast China) (Fig. S5e) and Peijiafen (North China) (Fig. S5f) for two industrial parks.
148 Second, compared to MEICv1.3, nearly 300 super-emitters seemed displaced in various degree, by at least one grid cell in
149 MEICv1.3 (i.e., $\sim 25 \times 25 \text{ km}^2$) (from the identified super-emitter centre), for example, Zhongjing (Southwest China) (Fig.
150 S5g) and Guolemude (Northwest China) (Fig. S5h). Third, the other super-emitters did not represent a localized maximum in
151 MEICv1.3 and were substantially underestimated compared to our results. They are essentially absent from the inventory
152 because their fluxes are at least one order of magnitude lower than our surveyed results. Notably, Nanzamu (Northeast China)
153 (Fig. S5i), Chengbei (Northwest China) (Fig. S5j), Tanjiazui (South China) (Fig. S5k), and Mengsheng (Southwest China)
154 (Fig. S5l) were captured by the one-year satellite observations. They represented the localized (i.e., $1 \sim 10 \text{ km}$) maximum but
155 were undoubtedly missed in the inventory.

156 Besides, the satellite-based study could capture the onset or the discontinuation of industrial activities unambiguously. New
157 or expanded super-emitters that emerged within the satellite measurements were found in this way. Correspondingly, the
158 satellite-based emission fluxes were significantly higher (at least one order) than the bottom-up estimations. For instance,
159 high NO_x emissions were observed over Xincheng (North China) (Fig. S6a) and Huagang (South China) (Fig. S6b). On the
160 other hand, industrial plant closures were also detected, for example, over Shidian (North China) (Fig. S6c) and over Hunhe
161 (Northeast China) (Fig. S6d). Therein the bottom-up emission inventory was likely outdated, overestimating the satellite-
162 based estimates by more than 100%.

163 Figure 4 shows the stable monthly variations (i.e., < 26%) in the satellite-based emission estimates of eight representative
164 super-emitters. The detailed variation information is shown in Fig. S7. Therefore, for most of the super-emitters, one-month
165 satellite overpasses could derive their yearly emission estimates and be capable of tracking their emission variations.

166 **Discussion**

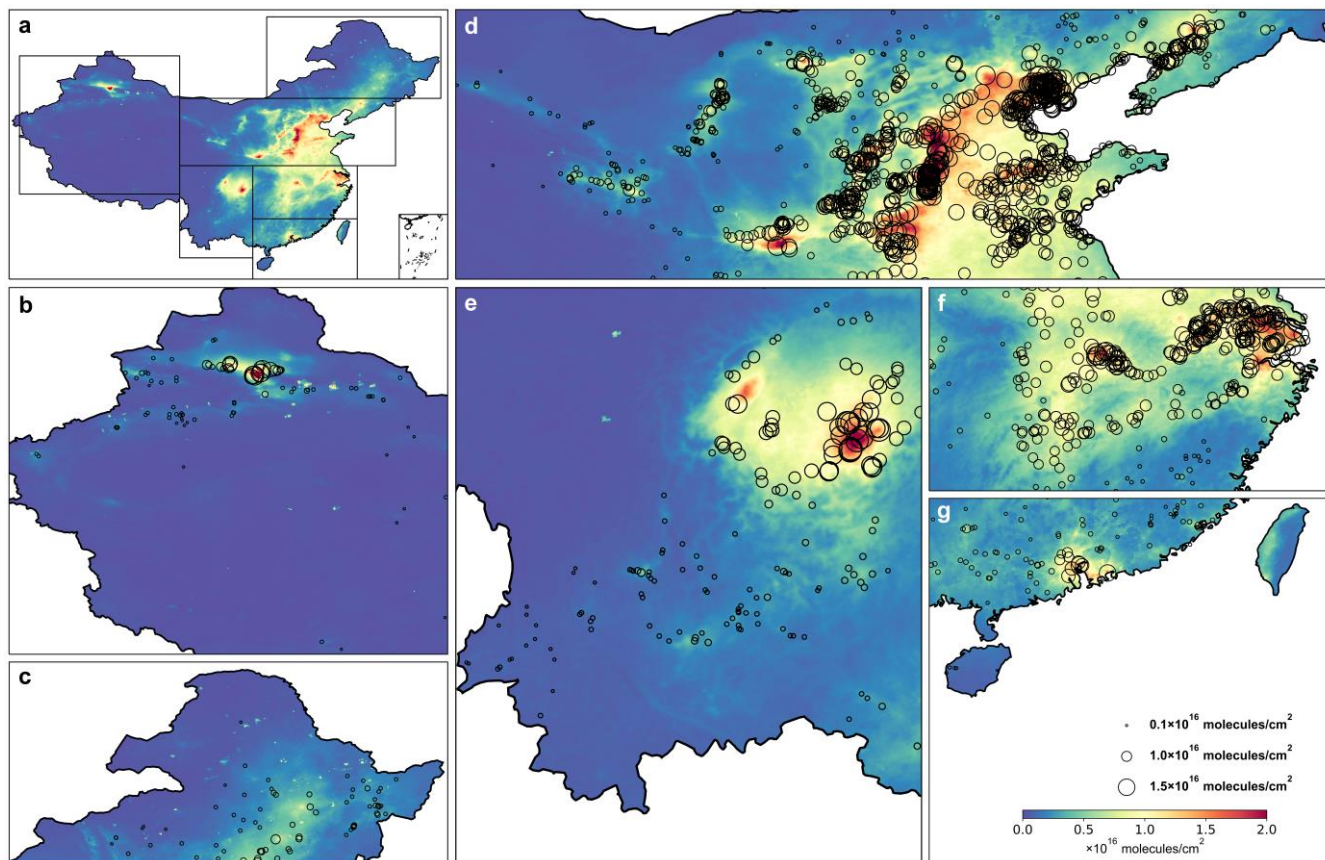
167 Here we develop an efficient, super-resolution inverse approach by collecting an entire year of daily TROPOMI
168 measurements, applying an oversampling method, and building a NO_x VCD-Transport-Lifetime-Emission model. The key
169 for preventing the smearing of the super-emitters is to exploit the super-resolution and wind-driven horizontal fluxes. This is
170 particularly useful for preserving strong gradients close to super-emitters even on top of considerably high pollution. In
171 contrast, current top-down approaches generally apply time-consuming inverse algorithms to satellite measurements, thus
172 sacrificing spatial resolution and focusing on regional issues²⁹. We compared our results with a state-of-the-art top-down
173 NO_x emission inventory²² for three representative super-emitters (Fig. S8). Although this inventory also relied on the
174 TROPOMI observations, it adopted another inverse model (i.e., the DESCO algorithm) to explore regional emission
175 variations on a 0.25° × 0.25° resolution. Figures S8 and S9 demonstrate that these two products were very similar in the
176 general spatial distributions and regional magnitude. In contrast, a key advance in this study was the considerable increase in
177 spatial resolution. Of particular relevance are the three super-emitters, which can only be distinguished in our results.

178 This work has presented a detailed and hyperfine inventory of NO_x super-emitters over China. They can be consistently
179 linked to either industrial hotspots or parks and responsible for the localized NO_x budget. More importantly, their emissions
180 are mostly underestimated, even displaced and missed, in a widely used emission inventory. This work can also capture the
181 emergence or closure of super-emitters in a relatively short time (i.e., monthly). Note that manual efforts regarding
182 distinguishing the super-emitters limit this study. Deep learning algorithms might be a prospective alternative that allows us
183 to rapidly and impartially identify super-emitters³⁰. To date, continuous emission monitoring systems (CEMS) remain
184 largely absent for super-emitters, particularly in industrial parks. Our results suggest that it is necessary to revisit traditional
185 bottom-up NO_x inventories. Otherwise, it is quite possible to mislead local air pollution distributions in CTMs and thus local
186 efforts for mitigation. By comparison, satellite surveys can make an important contribution to monitoring NO_x emissions,
187 particularly beneficial for up-to-date emission inventories for quickly developing countries. Therefore, widespread and

188 sustained deployment of a multi-tiered observational strategy, i.e., a combination of this hotspot detection technique with a
189 near-real-time ground-based and another satellite-based monitoring network of regional sources, could greatly advance
190 scientific understanding of NO_x budgets. More specifically, our approach, together with more comprehensive bottom-up
191 information, could be expanded to detect abnormal (e.g., leakage) facilities³¹ on a large spatial scale. More hyperfine
192 satellite-based measurements (e.g., GHGsat for methane, ~ 50 × 50 m²)^{32,33} might further facilitate the isolation and
193 identification of the super-emitters in intensive source regions.

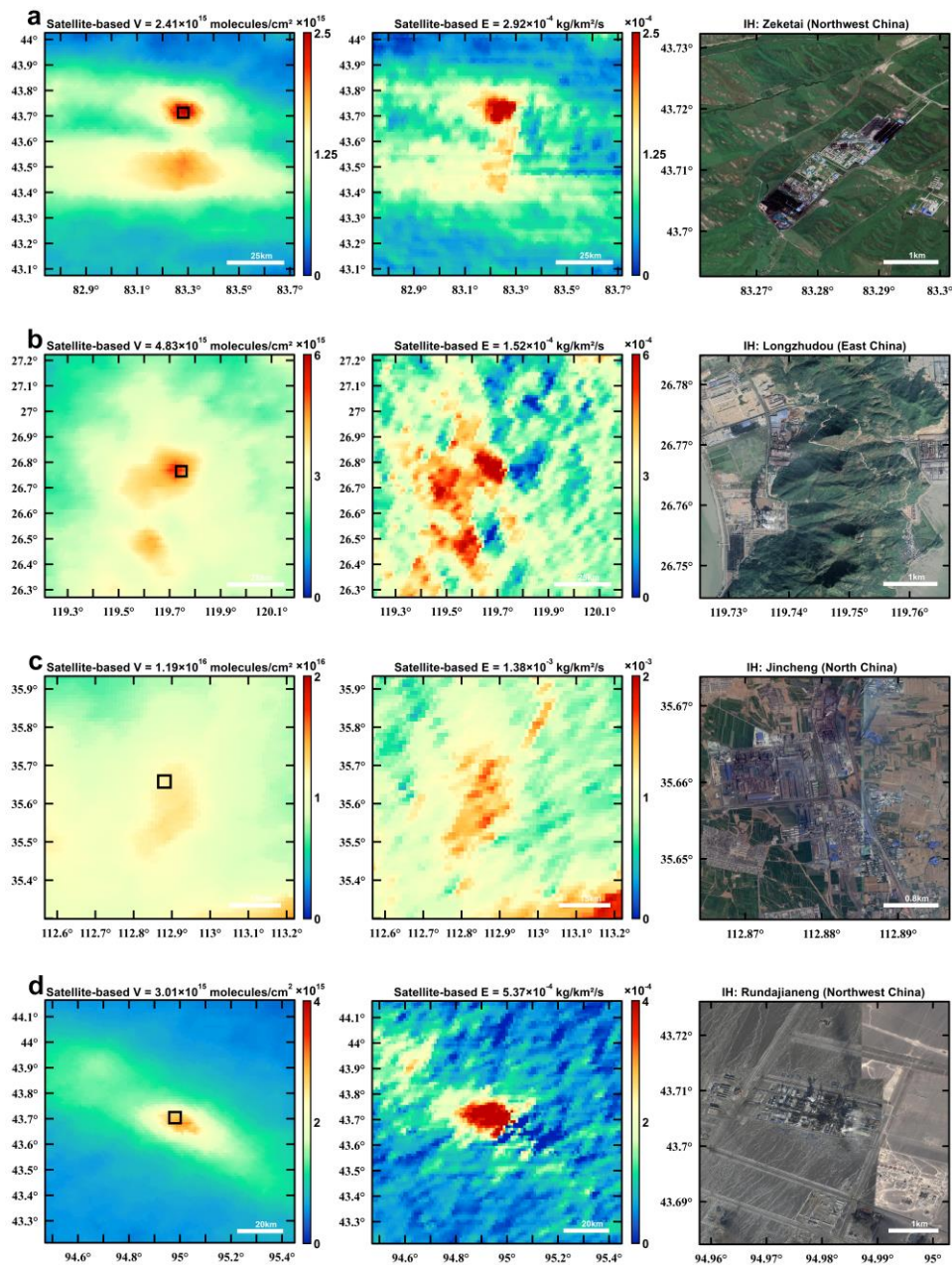
194

195



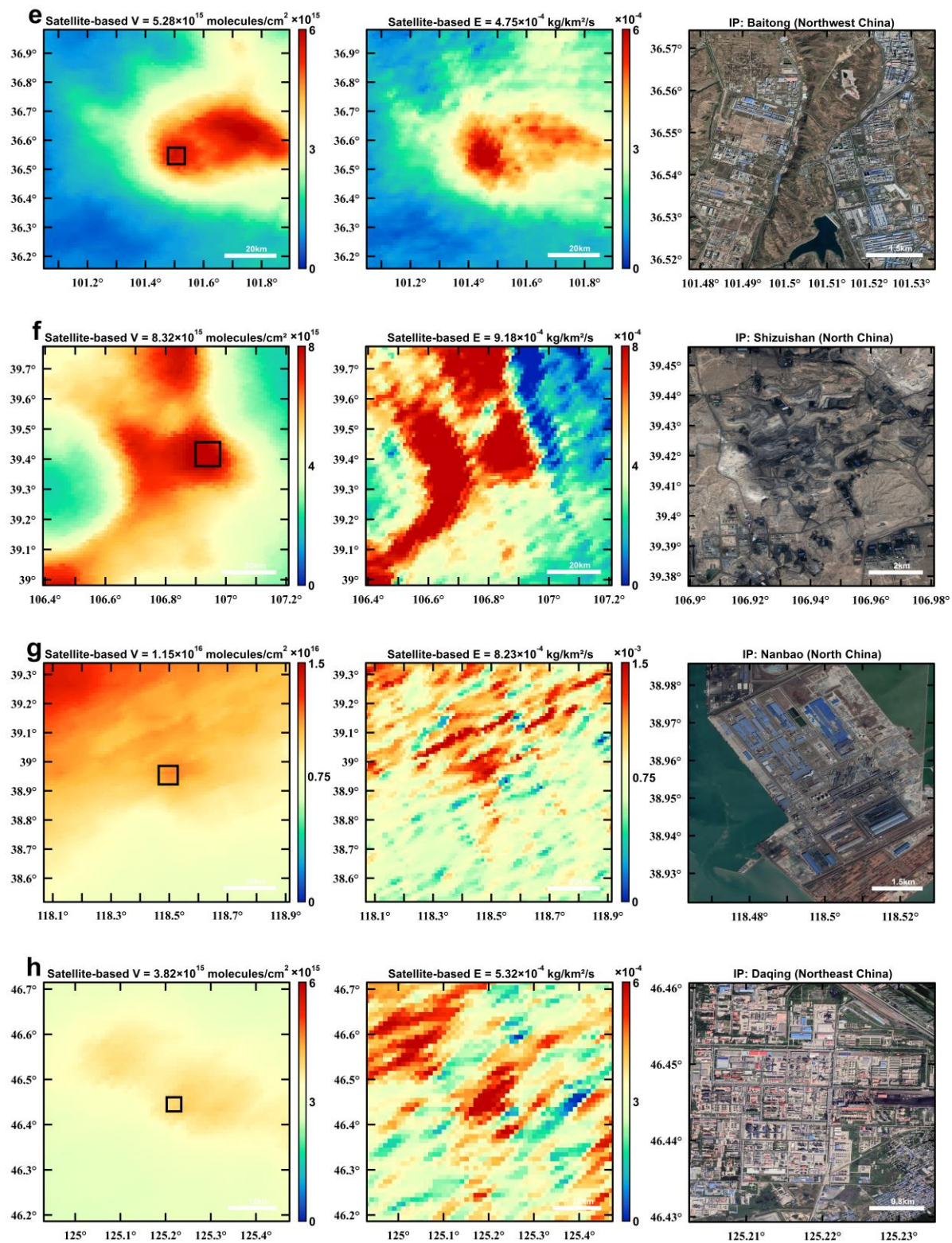
196

197 **Fig. 1. One-year oversampled NO_x VCDs and emission hotspots based on the TROPOMI instrument.** **a**, One-year
 198 oversampled NO_x VCDs across China. **b ~ g**, Zoom-ins over Northwest, Northeast, North, Southwest, East, and South China,
 199 which were marked by the black rectangles in Fig. 1a. Super-emitters are marked by black circles and scattered over China;
 200 their sizes denote the satellite-based emission fluxes. Detailed information of the super-emitters are recorded in
 201 Supplementary Tables 1 and 2 and Supplementary Map of the Super-emitters.

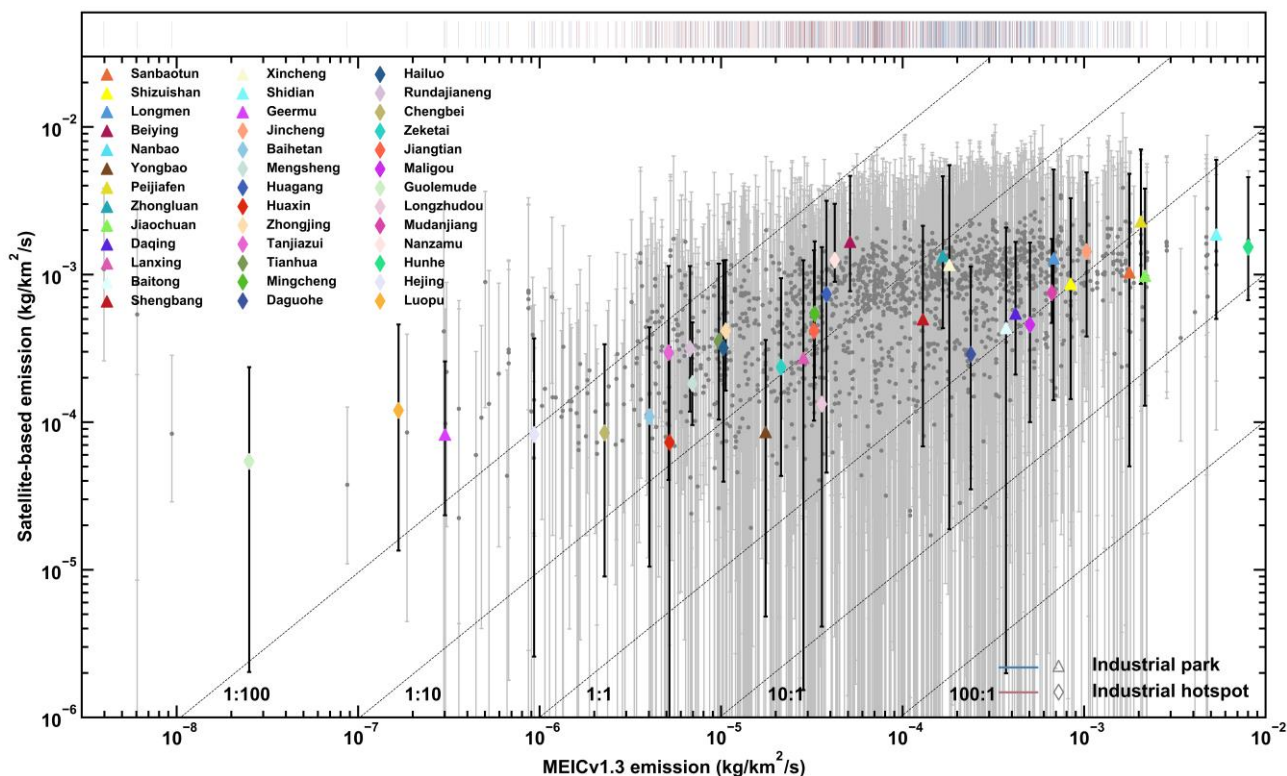


202

203 **Fig. 2. Illustrative examples of super-emitters, including industrial hotspots (IH) and parks (IP).** a ~ h, For each site,
 204 the left and medium panels offer the TROPOMI-based NO_x VCDs and emissions, respectively. The vertical and horizontal
 205 axes correspond to latitude and longitude, respectively. The right panels offer a close-up view of the super-emitters outlined
 206 by the black rectangles in the left panel. Satellite-based V and E denote the satellite-based VCDs and emissions, respectively.
 207 The satellite images come from the Landsat 8 imageries (**Fig. S2a ~ S2d**).



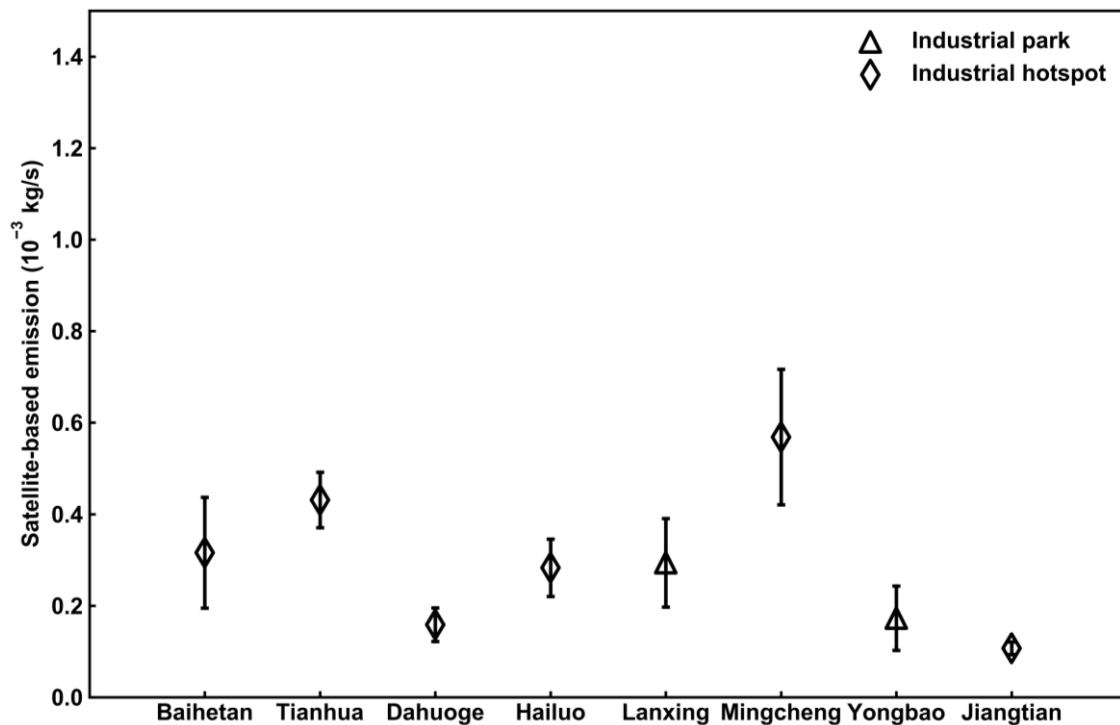
209 **Fig. 2. Illustrative examples of super-emitters, including industrial hotspots (IH) and parks (IP). a ~ h,** For each site,
210 the left and medium panels offer the TROPOMI-based NO_x VCDs and emissions, respectively. The vertical and horizontal
211 axes correspond to latitude and longitude, respectively. The right panels offer a close-up view of the super-emitters outlined
212 by the black rectangles in the left panel. Satellite-based V and E denote the satellite-based VCDs and emissions, respectively.
213 The satellite images come from the Landsat 8 imageries (**Fig. S2e ~ S2h**).



214

215 **Fig. 3. Satellite-derived NO_x emission fluxes versus a bottom-up emission inventory (MEICv1.3).** Satellite-based NO_x
 216 emission estimates for the cities (diamonds) and super-emitters, including industrial hotspots (triangles) and parks (circles)
 217 versus bottom-up NO_x emission estimates in MEICv1.3. To track the cities and super-emitters more clearly, we successively
 218 each one by a vertical line in the top panel. The five dashed oblique lines from left to right represent ratios of the MEIC-
 219 based emissions to the satellite-based emissions of 1:100, 1:10, 1:1, 10:1, and 100:1. The satellite-based emission fluxes are
 220 calculated assuming a baseline NO_x lifetime of 4 hours (Methods). The error bars correspond to upper- and lower-bound flux
 221 estimates based on a lifetime of 1 hour and 24 hours, respectively. Biomass-burning hotspots are omitted from this
 222 comparison, which are not included in MEICv1.3.

223



224

225 **Fig. 4. Representative examples of super-emitters that show stable monthly variations in the satellite-based NO_x**
226 **emissions.** The error bars represent 1-σ uncertainties.

227

228 Methods**229 Satellite observations**

230 The TROPOMI instrument on the European Space Agency's Sentinel-5P satellite provides daily global coverage of slant
231 column densities (SCDs) of NO₂ with an unprecedented spatial resolution of up to 3.5 × 7 km² (3.5 × 5.5 km² from August
232 2019 onward)^{7,13,34}. Its overpass time is close to noon (13:30 local time). The satellite measurements with a high resolution
233 allow us to analyze the finer scale spatiotemporal characteristics of NO₂. On this basis, the following calculation of
234 tropospheric NO₂ VCDs was very similar to the operational product³⁵, for which detailed algorithms can be found in the
235 production description³⁶. However, the difference was associated with the conversion of SCDs to VCDs that relied on the air
236 mass factor (AMF) approach. In the operational product, the a priori NO₂ profile was taken from the global chemistry
237 transport Tracer Model 5 (TM5-MP) with a spatial resolution of 1° × 1°. By comparison, we improved this process by using
238 a priori profile from a comparably high resolution (i.e., 5.5 × 5.5 km²) CTM (i.e., the WRF-CMAQ model^{37,38}). Note that
239 measurements with cloud fraction above 30% or a “qa value” (indicating data quality) below 0.75 were skipped³⁶. For each
240 pixel, to derive the lower VCD and eliminate the bias of the stratospheric estimate, we subtracted the 5th percentile within the
241 individual pixel from the total VCD⁷.

242 The WRF-CMAQ model

243 The two-way coupled WRF-CMAQ model (the WRF-CMAQ model) was applied to provide a priori profile and wind fields
244 on the spatial resolution of 5.5 × 5.5 km² (comparable to the resolution of the TROPOMI instrument). The results are the
245 foundation of the AMF calculation and the following top-down NO_x emission estimates. Detailed model settings can be
246 found in our previous papers^{39,40}. Meteorological initial and boundary conditions were obtained from the European Centre
247 for Medium-range Weather Forecasts (ECMWF) ERA5 reanalysis dataset with the spatial resolution of 1° × 1° and temporal
248 resolution of 6 hours. The analysis nudging option was switched on for temperature, humidity above the PBL, and winds at
249 all model levels, thus being nudged to the meteorological driving data (i.e., the ERA5 reanalysis dataset)⁴¹.

250 The horizontal domain of the model covered mainland China with a compatible horizontal resolution (5.5 × 5.5 km²)
251 following a Lambert Conformal Conic projection (Fig. 1a). In terms of the vertical configuration, 29 sigma-pressure layers
252 ranged from the surface to the upper-level pressure of 100 hPa, 20 layers of which are located below around 3 km to derive
253 finer meteorological and chemical characteristics within the planetary boundary layer.

254 The anthropogenic emissions were obtained from MEICv1.3¹⁵, which contained primary species (e.g., primary PM_{2.5}, SO₂,
255 NO_x, CO, and NH₃) from five anthropogenic sectors (i.e., agriculture, power plant, industry, residential, and transportation).
256 This inventory was initially designed with the spatial resolution of 0.25° × 0.25° and thus reallocated to match the domain
257 configuration (i.e., 5.5 × 5.5 km²) in the study.

258 **One-year oversampled tropospheric NO₂ VCDs**

259 To achieve a super-resolution reconstruction for the one-year tropospheric NO₂ VCDs, we applied the oversampling method
 260 to convert from the original satellite pixels to the 1 × 1 km² grid cells. As demonstrated in previous studies associated with
 261 reshaping air pollutant distributions, this technique can exploit the fact that the location, shape, and orientation of the satellite
 262 footprints slightly varies from one orbit to another^{14,18}. Thus, a much higher resolution can be obtained on the spatial
 263 distribution by sacrificing temporal information. This was distinct from the most widely used geometry methods that
 264 generally rely on interpolation or binning on a rectangular latitude-longitude grid⁴².
 265 Here the oversampling technique we adopted was similar to early attempts^{18,42,43}. Initially, a grid size of 1 × 1 km² was
 266 chosen. For each overpass, the TROPOMI footprint pixel coverage was calculated and, for computational reasons,
 267 approximated as an ellipse on a rectangular latitude–longitude grid. And then, we calculated the area-averaged value using
 268 all measurements overpassing the given cell. During this process, we also considered the influences of the footprint size that
 269 was set as a weight inversely proportional to the area of each footprint. Nevertheless, a measurement result would be
 270 regarded as erroneous values and thus eliminated when it was more than 10 standard deviations from the average¹⁸. As a
 271 result, 3.12% of the measurements were eliminated in this way.

272 **The top-down NO_x emission model**

273 We developed an efficient, super-resolution (i.e., 1 × 1 km²) top-down inverse model on the basis of the one-year
 274 oversampled TROPOMI NO₂ VCDs. This model took into account their chemical and meteorological loss, including
 275 chemical loss and horizontal transport. Therein the horizontal fluxes considered both time-averaged advection and diffusion
 276 processes⁷, while vertical fluxes, either upward or downward transport, were neglected, owing to their small contributions to
 277 the NO_x budget¹⁴. The latter assumption was used in numerous studies^{7,14}. This model was assumed to be equilibrium ($\frac{\partial V_{ij}}{\partial t} =$
 278 **0**), the governing equation of which was thus shown as follows (Eqs. 1 ~ 4):

$$279 \frac{\partial V_{ij}}{\partial t} = \mathbf{r} \mathbf{E}_{ij} - \frac{V_{ij}}{\tau_{ij}} - \mathbf{w}_{ij} \cdot \nabla V_{ij} + \nabla \cdot (\mathbf{k}_{ij} \cdot \nabla V_{ij}) = \mathbf{0} \text{ (Eq. 1)}$$

280 Therein V_{ij} represents the tropospheric NO₂ VCDs in the grid (i, j) of 1 × 1 km². \mathbf{E}_{ij} denotes all ground NO_x sources, which
 281 combines anthropogenic, soil, and biomass burning NO_x emissions. \mathbf{r} represents the ratio of NO₂ over NO_x concentration. In
 282 theory, the daytime NO_x chemical system reaches equilibrium rapidly and \mathbf{r} varies little. In this study, we set \mathbf{r} to be 0.76^{7,14}.
 283 The remaining terms in Eq. 1 represent the potential NO_x sinks, including chemical, deposition, horizontal, and diffusional
 284 loss. Given that the local overpass time of TROPOMI is close to noon (13:30 local time), the chemical NO_x sink is
 285 dominated by the chemical loss reaction of NO₂ with OH, which can be described by a first-order time constant τ_{ij} and, thus,
 286 can be estimated from the measured V_{ij} itself as $\frac{V_{ij}}{\tau_{ij}}$. τ_{ij} indicates the lifetimes associated with deposition and chemical loss
 287 in nature. In theory, instantaneous NO_x lifetime is dominated by several factors, such as ozone levels and actinic fluxes, and

288 also the NO_x concentration itself at the presence of high NO_x levels. As a result, the NO_x lifetime is linked with season and
 289 meteorological conditions. Therefore, the assumption of the NO_x lifetime is a major limitation of this method and might be
 290 inappropriate for super-emitters^{6,7,14,44}.

291 However, previous studies have demonstrated that the assumed lifetime could appropriately relate the measured $V_{i,j}$ to the
 292 actual emissions $E_{i,j}$ via mass balance. As shown in previous attempts in Riyadh, the NO_x lifetime has been derived to 4
 293 hours with an uncertainty of 35%⁶. Its seasonal variations were found to be weak. In the United States and China, a similar
 294 method was applied to cities and power plants, resulting in a mean lifetime of 3.8 ± 1.0 hours for May-September²³. In this
 295 study, we utilized a value of 4 hours for all regions. For many of the hotspots, there can be substantial transport out of the
 296 box, in which case the effective lifetime would be smaller than 4 hours. Given the high spatial resolution, the emission
 297 estimates of a grid cell derived in this way were more likely to be underestimated than overestimated. For specific remote
 298 sites, however, 4 hours could be too short.

299 Therefore, we applied conservative assumptions using lifetimes of 1 hour and 24 hours to provide upper- and lower-bound
 300 emission estimates. The corresponding uncertainties are considered and shown as error bars in Fig. 3. Although more
 301 sophisticated methods, like regional CTM simulations, are available, they would not significantly optimize the super-
 302 resolution emission estimates for the super-emitters. Alternatively, we could further introduce satellite-based HCHO VCDs
 303 into our framework to constrain the OH distributions⁴⁵, which might be useful for optimizing the model.

304 $\mathbf{w}_{i,j} \cdot \nabla V_{i,j}$ denotes the time-averaged advection term. Therein $\mathbf{w}_{i,j}$ represents the time-averaged wind vector, which is
 305 obtained from the WRF-CMAQ driven by the European Centre for Medium-range Weather Forecasts (ECMWF) ERA5
 306 dataset. $\nabla \cdot (\mathbf{k}_{i,j} \cdot \nabla V_{i,j})$ represents the diffusion term. Therein $\mathbf{k}_{i,j}$ is the diffusion coefficient tensor (in $\text{m}^2 \cdot \text{s}^{-1}$), which
 307 indicates the diffusion transport driven by the residual winds. This process could be simplified as follows (Eqs. 2 ~ 4):

$$308 \nabla \cdot (\mathbf{k}_{i,j} \cdot \nabla V_{i,j}) = \nabla \cdot (\mathbf{k}_i \cdot \nabla V_i) + \nabla \cdot (\mathbf{k}_j \cdot \nabla V_j) \text{ (Eq. 2),}$$

$$309 \mathbf{k}_i = \frac{1}{2}(\overline{\mathbf{w}_i})^2 \mathbf{t} \text{ (Eq. 3),}$$

$$310 \mathbf{k}_j = \frac{1}{2}(\overline{\mathbf{w}_j})^2 \mathbf{t} \text{ (Eq. 4).}$$

311 Therein \mathbf{k}_i and \mathbf{k}_j are the diffusion coefficients in the zonal and meridional directions, respectively. We applied a random
 312 walk assumption to derive the diffusion coefficients. The random walk step was assumed to be fixed and equal to the
 313 deviation of wind speed in the zonal or meridional direction ($\overline{\mathbf{w}_i}$ or $\overline{\mathbf{w}_j}$). \mathbf{t} is one hour, compatible to the sampling temporal
 314 interval of the simulated wind information.

315 Note that a background column was first subtracted from the NO_x VCDs, so as to include only the emission fluxes of the
 316 point sources responsible for the hotspots. The background column was estimated as the 5th percentile of all the $1 \times 1 \text{ km}^2$
 317 oversampled grids⁷. The background correction is illustrated in the Supplementary Information.

318 Emissions of super-emitters and cities were also calculated in MEICv1.3 and used to compare with our satellite-based
 319 emission estimates. For 2016, this bottom-up inventory was established at a spatial resolution of $0.25^\circ \times 0.25^\circ$ and of five

320 anthropogenic sectors (i.e., agriculture, power plant, industry, residential, and transportation). According to our super-
321 resolution results, the inventory was first re-gridded to the $1 \times 1 \text{ km}^2$ resolution. For the cities, the emissions in MEICv1.3
322 were then summed over all sectors, while, for the super-emitters, only those of industry and power plant sectors were
323 considered. Specifically, these super-emitters were attributed to industrial hotspots or parks, including the following sectors:
324 power industry, oil refineries, transformation industry, combustion for manufacturing, and process emissions during
325 production and application. Note that only the $1 \times 1 \text{ km}^2$ grids that contained the super-emitters were used to calculate the
326 averaged emission estimated.

327 For several reasons, MEICv1.3 may underestimate the emissions of the super-emitters even more than shown in Fig. 3. First,
328 the main reason, as explained above, is attributed to the NO_x lifetime, which could be smaller than the 4 hours we assumed,
329 directly resulting in an underestimation of our estimates. Second, depending on the thermal contrast, the TROPOMI
330 instrument, like any other infrared instrument, can miss the lower layer of the atmosphere in which NO_x is emitted. Hence,
331 our results are more likely to underestimate NO_x VCDs than to overestimate them.

332 **Identification and attribution**

333 By combining the tropospheric NO_2 VCDs, the top-down NO_x emission estimates, and the high-quality visible imageries
334 from Landsat 8, we identified the super-emitters manually. Although automated ways with uniform thresholds might result
335 in more consistent and flexible identifications, no satisfactory set of criteria was found that could be applied for the super-
336 emitters nationwide. This is mainly because, in localized regions, the NO_x budgets respond to the changes in not only the
337 super-emitters but also the background. In addition, the wildfire emergencies generally emitted elevated NO_x plumes and
338 especially hamper the identification of hotspots over a large area, even on a one-year average (for example, most of
339 Northeast and Southwest China)⁴⁶. We thus combined the MODIS fire product and the high-quality visible imageries to
340 eliminate the fire hotspots.

341 To identify the super-emitters manually, we identified the localized maxima of both VCDs and emissions, which was
342 significantly higher than the background value. Along with the visible imageries, we could attribute the characteristic
343 enhancement to an industrial hotspot or park. As a result, the typical area with a super-emitter could be identified with a
344 limited geographical scope (i.e., $< 5 \times 5 \text{ km}^2$). Each super-emitter was approximated as a rectangle on the latitude-longitude
345 grid, the central, minimum, and maximum coordinates of which were recorded in Supplementary Table 1. We must highlight
346 that, within densely source areas (e.g., megacities), the emission gradients from numerous super-emitters interfered with
347 each other and were inevitably missed.

348 Although the visible imageries enabled us to ascertain the locations of the super-emitters, it was not possible to identify the
349 industry type directly. Particularly, in China, where the industry is still rapidly developing, the associated bottom-up
350 information may not be assessable. In addition, the Baidu Map allowed us to assign a name to each super-emitter. The usual
351 choice was the name of the specific address recorded in Baidu Map or the name of the nearest geographical area.

352 **Reference**

- 353 1. Richter, A., Burrows, J. P., Nüß, H., Granier, C. & Niemeier, U. Increase in tropospheric nitrogen dioxide over
354 China observed from space. *Nature* **437**, 129–132 (2005).
- 355 2. Edwards, P. M. *et al.* High winter ozone pollution from carbonyl photolysis in an oil and gas basin. *Nature* **514**,
356 351–354 (2014).
- 357 3. Wang, J. *et al.* Fast sulfate formation from oxidation of SO₂ by NO₂ and HONO observed in Beijing haze. *Nat.*
358 *Commun.* **11**, 2844 (2020).
- 359 4. Zhang, R. *et al.* Formation of urban fine particulate matter. *Chem. Rev.* **115**, 3803–3855 (2015).
- 360 5. Martin, R. V *et al.* Global inventory of nitrogen oxide emissions constrained by space-based observations of NO₂
361 columns. *J. Geophys. Res. Atmos.* **108**, (2003).
- 362 6. Beirle, S., Boersma, K. F., Platt, U., Lawrence, M. G. & Wagner, T. Megacity emissions and lifetimes of nitrogen
363 oxides probed from space. *Science*. **333**, 1737–1739 (2011).
- 364 7. Beirle, S. *et al.* Pinpointing nitrogen oxide emissions from space. *Sci. Adv.* **5**, eaax9800 (2019).
- 365 8. Tong, D. *et al.* Targeted emission reductions from global super-polluting power plant units. *Nat. Sustain.* **1**, 59–68
366 (2018).
- 367 9. Tang, L. *et al.* Substantial emission reductions from Chinese power plants after the introduction of ultra-low
368 emissions standards. *Nat. Energy* **4**, 929–938 (2019).
- 369 10. Zheng, H. *et al.* Development of a unit-based industrial emission inventory in the Beijing-Tianjin-Hebei region and
370 resulting improvement in air quality modeling. *Atmos. Chem. Phys.* **19**, 3447–3462 (2019).
- 371 11. China, S. C. of the P. R. of. Air pollution prevention and control action plan. [http://www.gov.cn/zwqk/2013-](http://www.gov.cn/zwqk/2013-09/12/content_2486773.htm)
372 [09/12/content_2486773.htm](http://www.gov.cn/zwqk/2013-09/12/content_2486773.htm) (2013).
- 373 12. The Ministry of Ecology and Environment of China. Action plan for comprehensive control of air pollution in
374 Beijing-Tianjin-Hebei and surrounding areas in autumn and winter from 2017 to 2018. 7–143 (2017).
- 375 13. Griffin, D. *et al.* High-resolution mapping of nitrogen dioxide with TROPOMI: First results and validation over the
376 Canadian oil sands. *Geophys. Res. Lett.* **46**, 1049–1060 (2019).
- 377 14. Kong, H. *et al.* High-resolution (0.05° × 0.05°) NO_x emissions in the Yangtze River Delta inferred from OMI. *Atmos.*
378 *Chem. Phys.* **19**, 12835–12856 (2019).
- 379 15. Li, M. *et al.* MIX: a mosaic Asian anthropogenic emission inventory under the international collaboration framework
380 of the MICS-Asia and HTAP. *Atmos. Chem. Phys.* **17**, (2017).
- 381 16. Janssens-Maenhout, G. *et al.* HTAP_v2. 2: a mosaic of regional and global emission grid maps for 2008 and 2010 to
382 study hemispheric transport of air pollution. *Atmos. Chem. Phys.* **15**, 11411–11432 (2015).
- 383 17. McLinden, C. A. *et al.* Space-based detection of missing sulfur dioxide sources of global air pollution. *Nat. Geosci.* **9**,
384 496–500 (2016).

- 385 18. Van Damme, M. *et al.* Industrial and agricultural ammonia point sources exposed. *Nature* **564**, 99–103 (2018).
- 386 19. Tang, L. *et al.* Air pollution emissions from Chinese power plants based on the continuous emission monitoring
387 systems network. *Sci. Data* **7**, 325 (2020).
- 388 20. Zhang, Q. *et al.* NO_x emission trends for China, 1995–2004: The view from the ground and the view from space. *J.*
389 *Geophys. Res. Atmos.* **112**, (2007).
- 390 21. Levelt, P. F. *et al.* The ozone monitoring instrument. *IEEE Trans. Geosci. Remote Sens.* **44**, 1093–1101 (2006).
- 391 22. Ding, J. *et al.* Chinese NO_x emission reductions and rebound as a result of the COVID-19 crisis quantified through
392 inversion of TROPOMI NO₂ observations. (2020). doi:10.1002/essoar.10503145.1.
- 393 23. Liu, F. *et al.* NO_x emission trends over Chinese cities estimated from OMI observations during 2005 to 2015. *Atmos.*
394 *Chem. Phys.* **17**, 9261–9275 (2017).
- 395 24. Liu, J. *et al.* Air pollutant emissions from Chinese households: A major and underappreciated ambient pollution
396 source. *Proc. Natl. Acad. Sci.* **113**, 7756–7761 (2016).
- 397 25. Tao, S. *et al.* Quantifying the rural residential energy transition in China from 1992 to 2012 through a representative
398 national survey. *Nat. Energy* **3**, 567–573 (2018).
- 399 26. Zhang, Q. *et al.* Drivers of improved PM_{2.5} air quality in China from 2013 to 2017. *Proc. Natl. Acad. Sci.* (2019).
- 400 27. The Ministry of Ecology and Environment of China. *Action plan for comprehensive control of air pollution in*
401 *autumn and winter of 2020-2021 in Beijing-Tianjin-Hebei and its surrounding areas and the Fenwei plain.*
402 https://www.mee.gov.cn/xxgk/xxgk/xxgk03/202011/t20201103_806152.html (2020).
- 403 28. Guo, Y., Tian, J. & Chen, L. Managing energy infrastructure to decarbonize industrial parks in China. *Nat. Commun.*
404 **11**, 981 (2020).
- 405 29. Mijling, B. & R., J. van der A. Using daily satellite observations to estimate emissions of short-lived air pollutants on
406 a mesoscopic scale. *J. Geophys. Res. Atmos.* **117**, (2012).
- 407 30. Reichstein, M. *et al.* Deep learning and process understanding for data-driven Earth system science. *Nature* **566**,
408 195–204 (2019).
- 409 31. Pandey, S. *et al.* Satellite observations reveal extreme methane leakage from a natural gas well blowout. *Proc. Natl.*
410 *Acad. Sci.* **116**, 26376 – 26381 (2019).
- 411 32. Varon, D. J., Jacob, D. J., Jervis, D. & McKeever, J. Quantifying Time-Averaged Methane Emissions from
412 Individual Coal Mine Vents with GHGSat-D Satellite Observations. *Environ. Sci. Technol.* **54**, 10246–10253 (2020).
- 413 33. Varon, D. *et al.* Satellite Discovery of Anomalously Large Methane Point Sources From Oil/Gas Production.
414 *Geophys. Res. Lett.* **46**, (2019).
- 415 34. Goldberg, D. L. *et al.* Enhanced Capabilities of TROPOMI NO₂: Estimating NO_x from North American Cities and
416 Power Plants. *Environ. Sci. Technol.* **53**, 12594–12601 (2019).

- 417 35. TROPOMI ATBD of the total and tropospheric NO₂ data products.
418 <https://sentinel.esa.int/documents/247904/2476257/Sentinel-5P-TROPOMI-ATBD-NO2-data-products>.
- 419 36. TROPOMI ATBD of the total and tropospheric NO₂ data products.
- 420 37. Wong, D. C. *et al.* WRF-CMAQ two-way coupled system with aerosol feedback: software development and
421 preliminary results. *Geosci. Model Dev.* **5**, 299–312 (2012).
- 422 38. Yu, S. *et al.* Aerosol indirect effect on the grid-scale clouds in the two-way coupled WRF-CMAQ: model description,
423 development, evaluation and regional analysis. *Atmos. Chem. Phys. Discuss.* 25649 (2013).
- 424 39. Wang, L. *et al.* Significant wintertime PM_{2.5} mitigation in the Yangtze River Delta, China from 2016
425 to 2019: observational constraints on anthropogenic emission controls. *Atmos. Chem. Phys. Discuss.* **2020**, 1–31
426 (2020).
- 427 40. Mehmood, K. *et al.* Relative effects of open biomass burning and open crop straw burning on haze formation over
428 central and eastern China: modeling study driven by constrained emissions. *Atmos. Chem. Phys.* **20**, 2419–2443
429 (2020).
- 430 41. Li, X. *et al.* The impact of observation nudging on simulated meteorology and ozone concentrations during
431 DISCOVER-AQ 2013 Texas campaign. *Atmos. Chem. Phys.* **16**, 3127–3144 (2016).
- 432 42. Sun, K. *et al.* A physics-based approach to oversample multi-satellite, multispecies observations to a common grid.
433 *Atmos. Meas. Tech.* **11**, 6679–6701 (2018).
- 434 43. Fioletov, V. E., McLinden, C. A., Krotkov, N., Moran, M. D. & Yang, K. Estimation of SO₂ emissions using OMI
435 retrievals. *Geophys. Res. Lett.* **38**, (2011).
- 436 44. Laughner, J. L. & Cohen, R. C. Direct observation of changing NO_x lifetime in North American cities. *Science.* **366**,
437 723–727 (2019).
- 438 45. Wolfe, G. M. *et al.* Mapping hydroxyl variability throughout the global remote troposphere via synthesis of airborne
439 and satellite formaldehyde observations. *Proc. Natl. Acad. Sci.* **116**, 11171–11180 (2019).
- 440 46. Mehmood, K. *et al.* Relative effects of open biomass burning and open crop straw burning on haze formation over
441 central and eastern China: modeling study driven by constrained emissions. *Atmos. Chem. Phys.* **20**, 2419–2443
442 (2020).

443 **Data availability.**

444 The TROPOMI data is available in <https://scihub.copernicus.eu/>. The DECSO-based NO_x emission is obtained from
445 <https://www.temis.nl/emissions/data.php>. The MEICv1.3 is from <http://meicmodel.org/>. The ERA5 meteorological
446 reanalysis dataset comes from <https://www.ecmwf.int/en/forecasts/datasets/reanalysis-datasets/era5>. The Landsat 8 data is
447 available in <https://developers.google.com/earth-engine/datasets/catalog/landsat-8>. Additional data related to this paper may
448 be requested from the authors.

449 **Supplementary materials.**

450 Supplementary information is available online.

451 **Author contributions.**

452 P.L. and C. W. designed this study and wrote the manuscript. P.L. and Y.P. developed the retrieval algorithm. P.L., P. S.,
453 L.D., M. L., N. X., J. L., S. L., and Y.L. derived the hyperfine maps and performed the analysis. C. W., J. M., X. Z., W. W.,
454 Y. S., W. S., G. W., L. W., X. C., Y. X., L. J., Y. Z., M. L., Z. L., and W. L. contributed to the discussions. S. Y., R. D., and
455 J.H.S contributed to the manuscript and supervised the research.

456 **Competing interests.**

457 The authors declare no competing interests.

458 **Acknowledgements.**

459 We thank ESA and the S-5P/TROPOMI level 1 and level 2 teams for the great work on initiating and realizing TROPOMI
460 data. This study is supported by National Natural Science Foundation of China (No. 22006030, 22076172, 21577126 and
461 41561144004), Hebei Youth Top Fund (BJ2020032), Research Fund of Education Bureau of Hebei (QN2019184), Initiation
462 Fund of Hebei Agricultural University (412201904 and YJ201833), the Department of Science and Technology of China
463 (No. 2016YFC0202702, 2018YFC0213506 and 2018YFC0213503), National Research Program for Key Issues in Air
464 Pollution Control in China (No. DQGG0107).

Figures

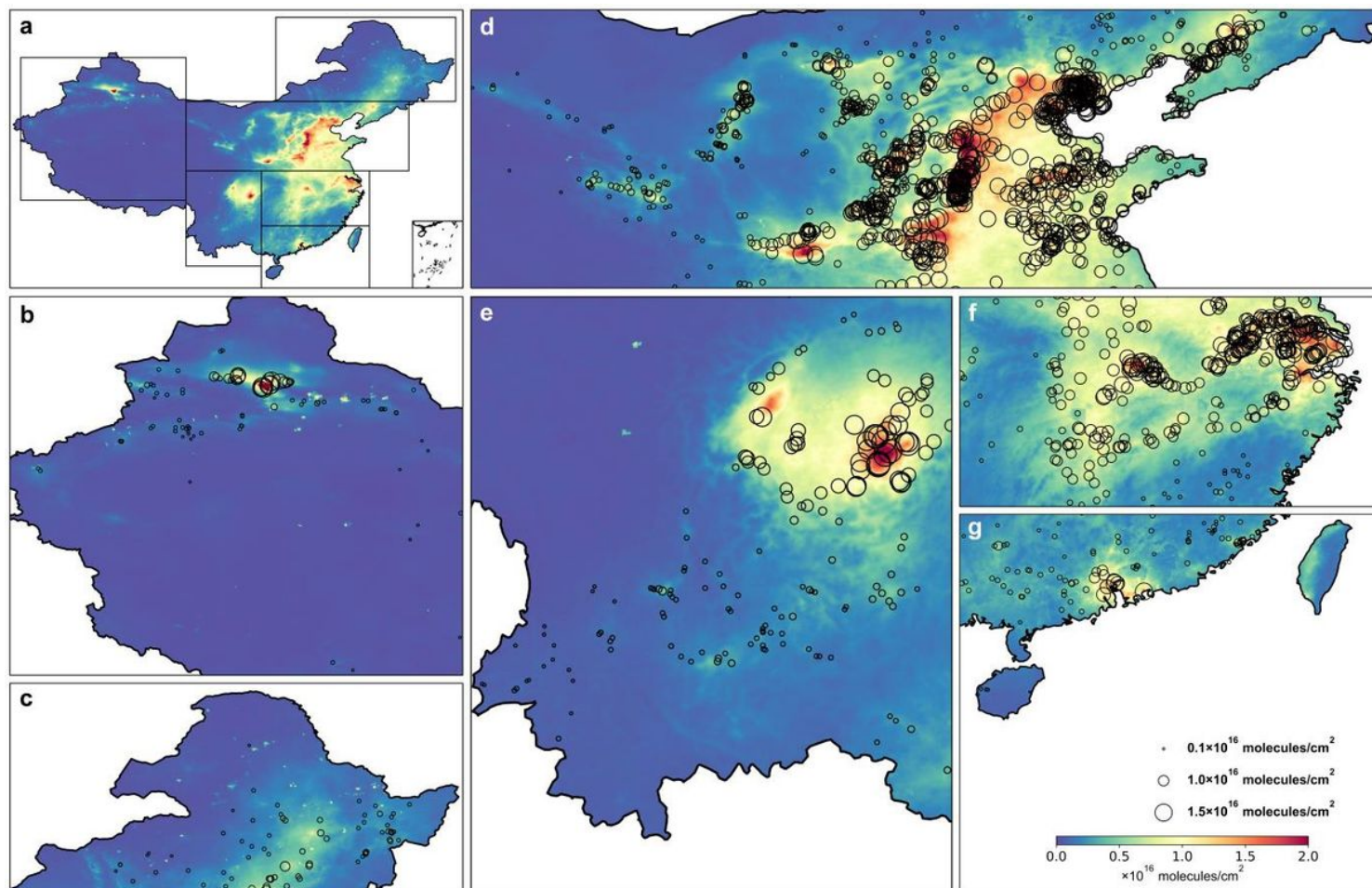


Figure 1

One-year oversampled NO_x VCDs and emission hotspots based on the TROPOMI instrument. a, One-year oversampled NO_x VCDs across China. b ~ g, Zoom-ins over Northwest, Northeast, North, Southwest, East, and South China, which were marked by the black rectangles in Fig. 1a. Super-emitters are marked by black circles and scattered over China; their sizes denote the satellite-based emission fluxes. Detailed information of the super-emitters are recorded in Supplementary Tables 1 and 2 and Supplementary Map of the Super-emitters.

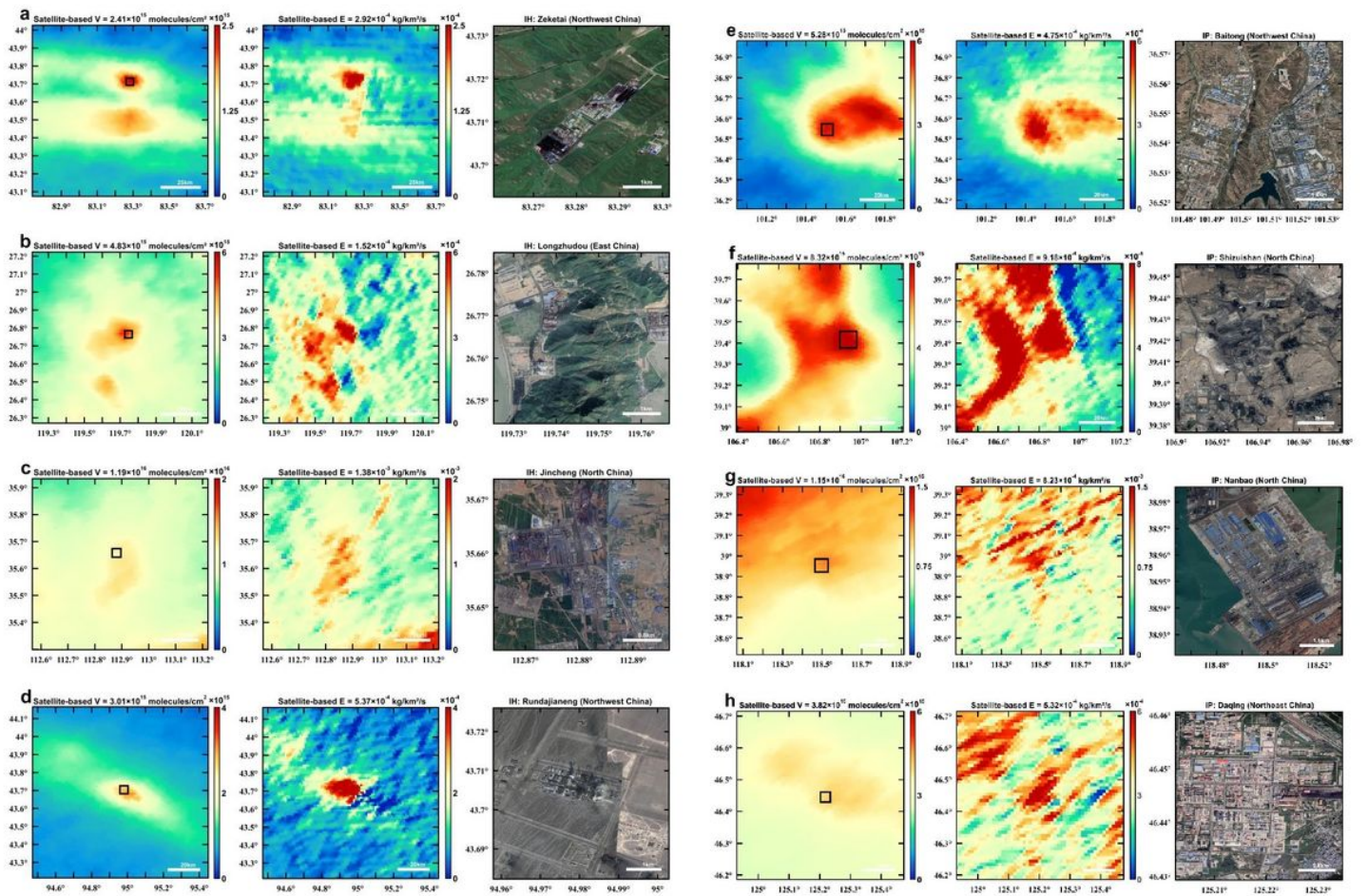


Figure 2

Illustrative examples of super-emitters, including industrial hotspots (IH) and parks (IP). a ~ h, For each site, the left and medium panels offer the TROPOMI-based NO_x VCDs and emissions, respectively. The vertical and horizontal axes correspond to latitude and longitude, respectively. The right panels offer a close-up view of the super-emitters outlined by the black rectangles in the left panel. Satellite-based V and E denote the satellite-based VCDs and emissions, respectively. The satellite images come from the Landsat 8 imageries (Fig. S2a ~ S2d). Illustrative examples of super-emitters, including industrial hotspots (IH) and parks (IP). a ~ h, For each site, the left and medium panels offer the TROPOMI-based NO_x VCDs and emissions, respectively. The vertical and horizontal axes correspond to latitude and longitude, respectively. The right panels offer a close-up view of the super-emitters outlined by the black rectangles in the left panel. Satellite-based V and E denote the satellite-based VCDs and emissions, respectively. The satellite images come from the Landsat 8 imageries (Fig. S2e ~ S2h).

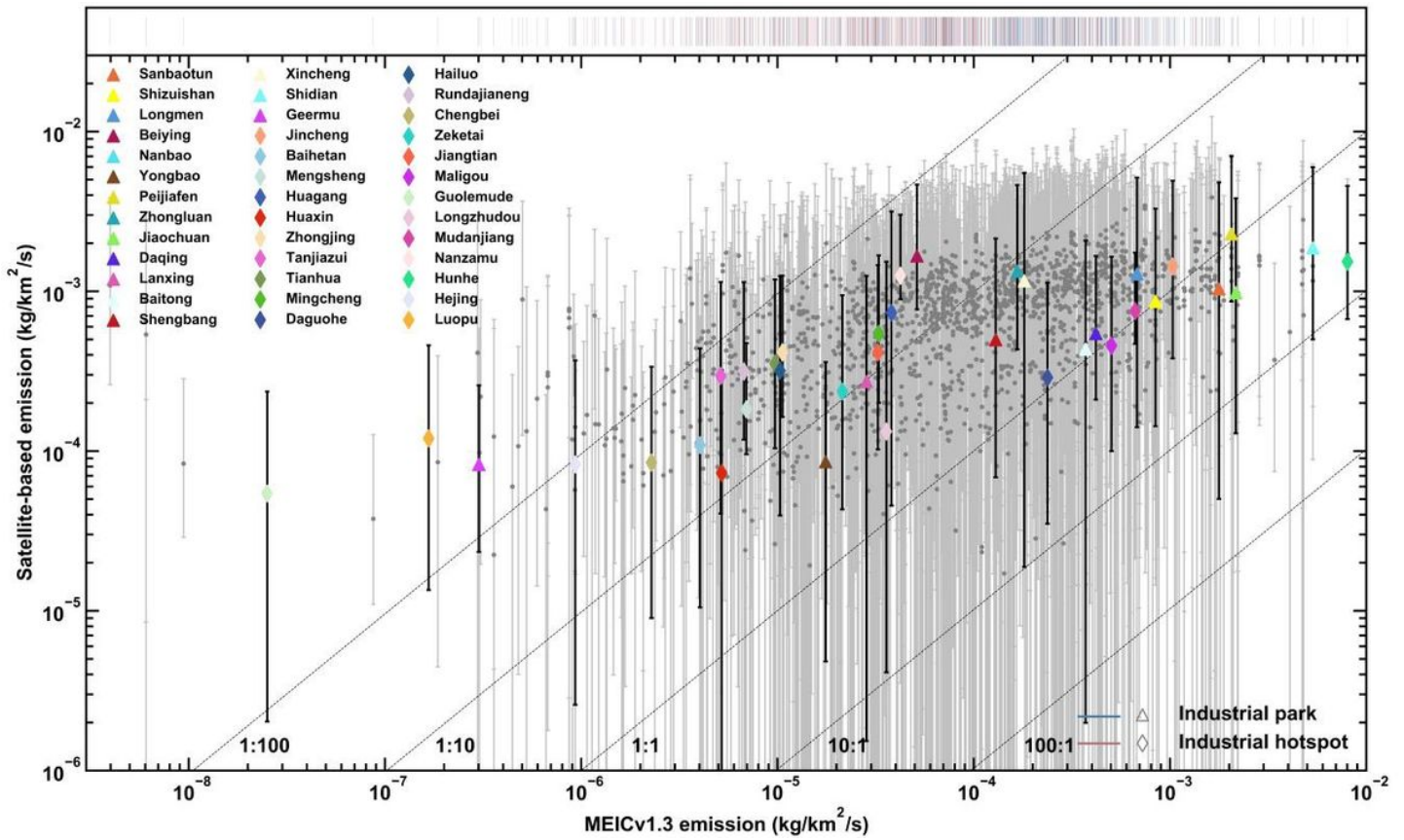


Figure 3

Satellite-derived NOx emission fluxes versus a bottom-up emission inventory (MEICv1.3). Satellite-based NOx emission estimates for the cities (diamonds) and super-emitters, including industrial hotspots (triangles) and parks (circles) versus bottom-up NOx emission estimates in MEICv1.3. To track the cities and super-emitters more clearly, we successively each one by a vertical line in the top panel. The five dashed oblique lines from left to right represent ratios of the MEIC-based emissions to the satellite-based emissions of 1:100, 1:10, 1:1, 10:1, and 100:1. The satellite-based emission fluxes are calculated assuming a baseline NOx lifetime of 4 hours (Methods). The error bars correspond to upper- and lower-bound flux estimates based on a lifetime of 1 hour and 24 hours, respectively. Biomass-burning hotspots are omitted from this comparison, which are not included in MEICv1.3.

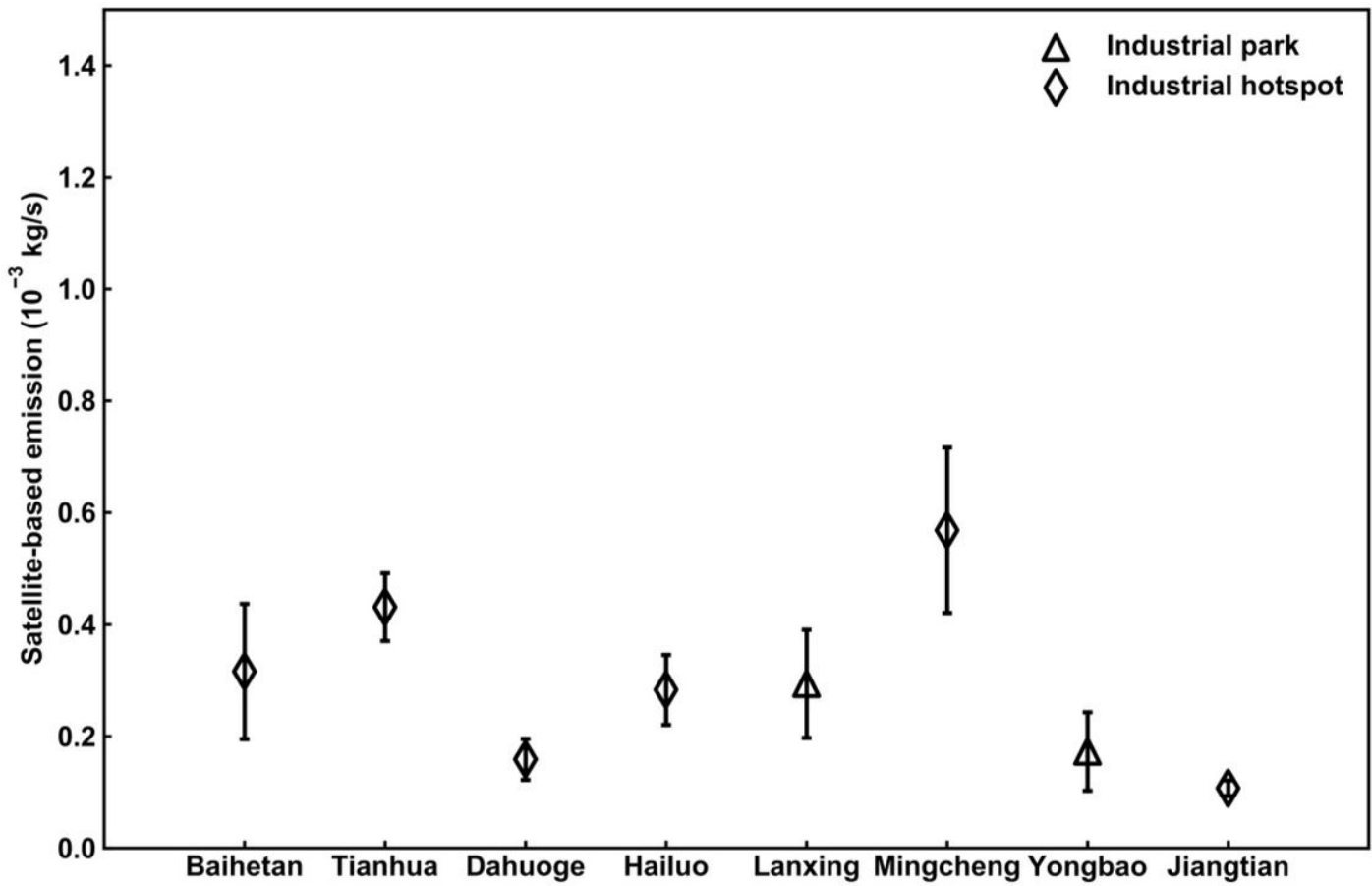


Figure 4

Representative examples of super-emitters that show stable monthly variations in the satellite-based NO_x emissions. The error bars represent 1-σ uncertainties.

Supplementary Files

This is a list of supplementary files associated with this preprint. Click to download.

- [SupplementaryInformation.pdf](#)
- [SupplementaryTable1.xlsx](#)
- [SupplementaryTable2.xlsx](#)
- [Mapofsuperemitters.zip](#)